

An optics-free single-pixel spectrometer using a broadband and tunable dynamic detector

Authors

Ling-Dong Kong¹, Qing-Yuan Zhao^{1,2*}, Hui Wang¹, Hai-Yang-Bo Lu¹, Hao Hao¹, Shu-Ya Guo¹, Xue-Cou Tu^{1,2}, La-Bao Zhang^{1,2}, Xiao-Qing Jia^{1,2}, Lin Kang^{1,2}, Xing-Long Wu³, Jian Chen^{1,2*}, and Pei-Heng Wu^{1,2}

Affiliations

¹Research Institute of Superconductor Electronics (RISE), School of Electronic Science and Engineering, Nanjing University, Nanjing, Jiangsu 210023, China.

²Purple Mountain Laboratories, Nanjing, Jiangsu 211111, China.

³National Laboratory of Solid State Microstructures and Department of Physics, Nanjing University, Nanjing, 210023, China

*Correspondence authors. Email: qyzhao@nju.edu.cn; chenj63@nju.edu.cn

Abstract

Optical spectrometers are the central instruments for exploring the interaction between light and matter. The current pursuit is to design a spectrometer without the need for wavelength multiplexing optics to effectively reduce the complexity and size of the hardware. Based on computational spectroscopic results and combining a broadband-responsive dynamic detector, we successfully demonstrate an optics-free single-pixel spectrometer which maps the tunable quantum efficiency of a superconducting nanowire into an ill-conditioned matrix to build a solvable reverse mathematical equation. Such a spectrometer can realize a broadband spectral responsivity ranging from 600 to 2000 nm. The spectral resolution at the telecom is 6 nm, exceeding the energy resolving capacity of existing infrared single-photon detectors. Meanwhile, benefiting from the optics free setup precise time-of-flight measurements can be simultaneously achieved. This work provides a revolutionary way for building multifunctional spectrometers, which can be upgraded to a hyperspectral camera straightforwardly with detector arrays.

MAIN TEXT

Introduction

Optical spectroscopy is a widely used technique to investigate wavelength-dependent interactions between light and matter across countless cutting-edge research fields(1-3) and industrial processes(4), where spectrometers are the central instruments (5). In conventional spectrometers, the incident light passes through spectral multiplexing optics to separate spectral components either at different times or different locations. Therefore, the information about the spectral intensity distribution can be known after measuring each spectral component by a photodetector or a detector array. Although the measurement step is straightforward, distinguishably separating wavelengths over spatial or temporal dimensions requires high-quality grating, prisms, or tunable bandpass filters. Thus, the bandwidth and resolution of a conventional spectrometer are limited by these complex wavelength multiplexing optics, especially for a system requiring a simplified configuration.

With a photon-counting detector of energy resolving capacity, a spectrometer can be simplified to a single-pixel and wavelength multiplexing optics can be removed. For instance, superconducting transition edge sensors (TESs) that are used widely in X-ray spectroscopy have single-photon sensitivity and the output amplitude is proportional to the energy of photon energy(6). Thus, TESs can be used as a single-pixel spectrometer by counting the photon counts and measuring the pulse amplitude(7). However, although very sensitive and low noise cryogenic readout electronics are applied, the energy resolution of a TES is limited to be ~ 0.15 eV (equivalent to a 245 nm wavelength resolution between 1305 nm and 1550 nm) for infrared photons(8), which is not fine enough for building a SPS for measuring visible and infrared spectra.

Computational spectrometers use a different approach to get the spectral information of incident light and give much more freedom in designing optics and choosing detectors(9). Different from a conventional spectrometer, the spectral component is no longer required to be derived from a single-shot measurement. Instead, each measurement could be a superposed response from a broadband incident light with an unknown spectrum \mathbf{x} . By conducting a group measurement \mathbf{y} , \mathbf{x} can be reconstructed by computing the reverse problem of $\Phi \mathbf{x} = \mathbf{y}$, where Φ is a calibrated two-dimensional matrix containing the spectral information of the system. In a computational spectrometer, the key is to build a linearly independent Φ and optimize the reconstruction algorithm accordingly. Previous works for building Φ are based on a filter array of varied optical transmission(9-12), a tunable optics by time multiplexing(13-15), or a detector array of varied spectral responsivity(16-18) (see Fig. S7 for a comparison between different approaches).

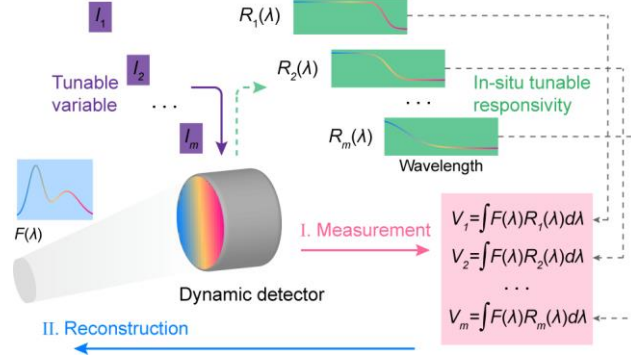


Fig. 1. Single-pixel spectrometer with a dynamic detector. The spectrometer is built on a dynamic detector whose internal spectral responsivity $R(\lambda)$ can be modulated by its bias I or other tunable variables. Unknown spectrum $F(\lambda)$ illuminates the detector directly. By tuning the bias, a sequence of measurements V is collected, which is the raw data for reconstructing $F(\lambda)$ computationally.

Here, we build a single-pixel spectrometer (SPS) based on a dynamic detector and a computational spectroscopy method as shown in Fig.1. While single-photon detectors with fine energy resolving capacity are rare, dynamic detectors whose spectral responsivity can be in-situ modulated electrically already exist in various detectors made from semiconductors(19, 20), superconductors(21, 22), and 2D materials(23). In this work, we choose a superconducting nanowire single-photon detector (SNSPD) as an example. As shown in Fig.1, the spectral responsivity of this dynamic detector depends on both the wavelength and the bias, which naturally contributes to a programmable Φ . By sweeping its bias current and collecting outputs, the forward mathematic equations can be built. Accompanied with a computational algorithm, the unknow spectrum is then reconstructed. Since no wavelength multiplexing optics are required, the proposed dynamic SPS fully utilizes the broadband response of the detector. Experimentally, we have demonstrated both monochromic and broadband spectral spectra from 600 nm to 2000 nm. Potential extension of the range to X-ray(24), ultraviolet(25), and longer wavelength(22) can be expected reasonably based on the recent developments of superconducting nanowire detectors. As electrical modulation is used, a large-size Φ (i.e. 81×81 in our experiments) can be generated straightforwardly without the need for complex readout for detector arrays proposed in previous works(9-12, 15-18). Consequently, a high spectral resolution of sub-10 nm is obtained at the telecom band.

Results

A superconducting nanowire single-photon detector is a photon-counting detector. It has wide spectral responsivity from ultraviolet(25) to mid-infrared(21, 22), single-photon sensitivity, high dynamic range, and the ability of on-chip integration with nanophotonic circuits(26). To enable the single-pixel spectrometer, the detector's responsivity needs to have linearly independent spectral features during the dynamic modulation. It is demonstrated both experimentally and theoretically that the quantum efficiency of an SNSPD has a strong dependence on its bias current I_b and the wavelength λ of the incident light(21, 22, 27). We fabricated a polarization-insensitive SNSPD (Fig. 2A) and calibrated the system spectral responsivity $\varphi_i(\lambda)$ including the tunable quantum efficiency of the nanowire and the coupling efficiency at each bias current I_b to build the responsivity

matrix Φ as shown in Fig. 2B. Fig. 2C shows that under low bias current photons of short wavelength can be detected with higher probability. When the bias current increasing, the responsive spectrum extends to longer wavelength. Therefore, $\varphi_i(\lambda)$ can be modulated continuously over a wide wavelength range simply by changing I_B .

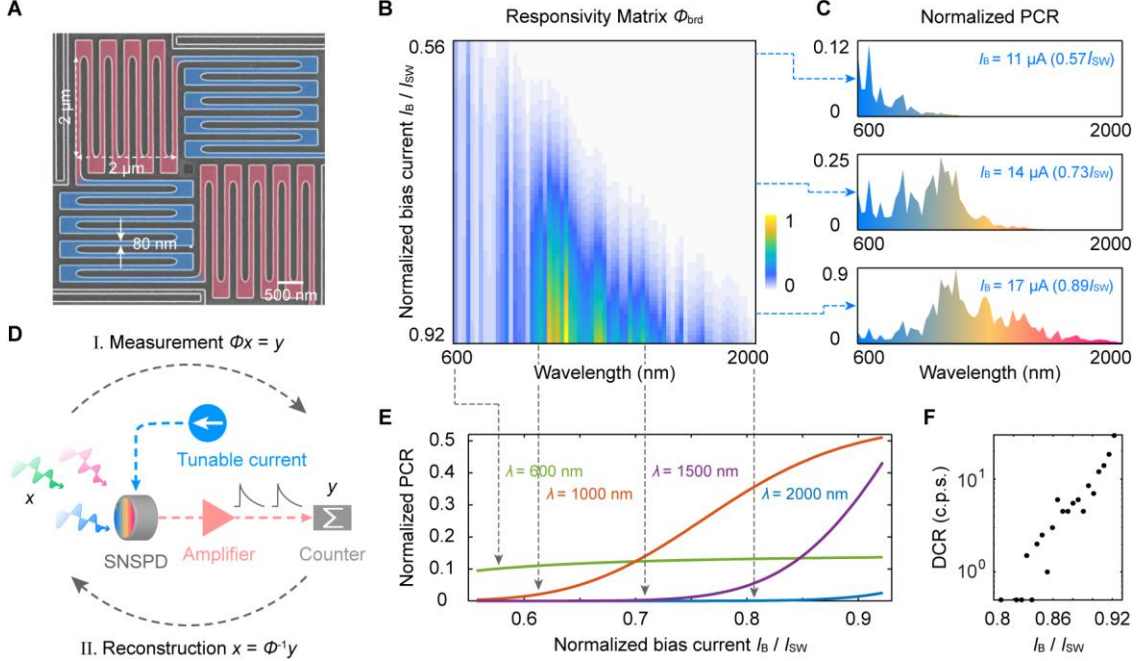


Fig. 2. Superconducting nanowire single-pixel spectrometer. (A) A scanning electron micrograph of the SNSPD, which meandered in perpendicular directions to remit photon polarization sensitivity (painted with two different colors). (B) The broadband calibrated responsivity matrix Φ_{brd} as a function of wavelength and bias current. The data is normalized to the maximum photon count rate. (C) The dependence of Φ_{brd} on I_B at fixed λ . (D) Operating principle diagram. (E) The dependence of Φ_{brd} on λ at fixed I_B . (F) Dark count rate versus bias current.

As illustrated in Fig. 2D, the single-pixel spectrometer measured spectral information through two steps—measurement and reconstruction. First, the photon count rates (PCR) c_i were collected as bias current increased with m steps. By discretizing $F(\lambda)$ and $\varphi_i(\lambda)$ into $F(k)$ and $\varphi_i(k)$ ($k = 1, 2, 3, \dots, n$), we obtain

$$c_i = \sum_{k=1}^m \varphi_i(k) F(k) \quad (1)$$

Assuming

$$\Phi = \begin{bmatrix} \varphi_1(1) & \varphi_1(2) & \dots & \varphi_1(n) \\ \varphi_2(1) & \varphi_2(2) & \dots & \varphi_2(n) \\ \vdots & \vdots & \ddots & \vdots \\ \varphi_m(1) & \varphi_m(2) & \dots & \varphi_m(n) \end{bmatrix}, \mathbf{x} = [F(1), F(2), \dots, F(n)]^T, \text{ and } \mathbf{y} = [c_1, c_2, \dots, c_m]^T,$$

the measurement process can be modeled discretely as

$$\Phi \mathbf{x} = \mathbf{y} \quad (2)$$

Each row of the matrix Φ represents a system spectral responsivity at different bias currents. For each wavelength, i.e., in each column of the matrix Φ , the PCR versus bias current is a sigmoidal curve as shown in Fig. 2E. For shorter wavelength light, the sigmoidal curve goes to saturate at an earlier inflection point of the bias current and the growth is faster than the light of longer wavelength. The measured PCR c_i versus bias current of the incident light that contains multiple wavelengths is the linear superposition of a series of PCR curves at the corresponding wavelengths with different weights. The dependence of the dark counts on bias current is also calibrated, which is shown in Fig. 2F. The dark count rate of the SNSPD is below 30 cps, which is an ultralow value compared to the overall photon counts during the experiments.

The reconstruction algorithm aims to reliably estimate the target spectrum \mathbf{x} from the measured \mathbf{y} and the prior knowledge Φ . Notably, the condition number of the matrix Φ is extremely large, which implies the spectral reconstruction of \mathbf{x} is an ill-posed problem(9, 16, 28), where the results are sensitive to perturbations of data due to noise. Thus, we minimized the measurement uncertainty by stabilizing the operating temperature with a fluctuation of less than 0.3 mK (Fig. S3), amplifying the detector's output with a cryogenic amplifier to reduce electrical readout noise and accumulating photon counts for a relatively long time to reduce photon counting noise. Moreover, the construction algorithm uses a regularization strategy. Here, we used a truncated generalized singular value decomposition (TGSVD) method to reduce the influence of perturbations during the reconstruction, which is a popular solver for the regularized solution of ill-posed inverse problems in imaging processing and machine learning(28).

Following the above workflow, we demonstrated the capability and performance of the computational single-pixel spectrometer by measuring and reconstructing different incident-light spectra from both monochromatic light sources and broadband light sources. The light was coupled to the SNSPD through a multimode fiber. Results for the free-space coupling setup were given in Fig. S4-S6. In our experiments, we calibrated two matrices of the system spectral responsivity, which are Φ_{brd} (Fig.2B) for broadband spectral measurement and Φ_{tel} (Fig.4A) for spectral measurement at telecom band. There are some fine features in the spectral responsivity, which are mainly due to the interference generated by multiple reflections at the detector and the use of incident light of a relatively long coherent length.

Φ_{brd} has a size of 71×71 . We used a broadband supercontinuum source (YSL SC-PRO-M) with an acoustic-optical tunable filter (AOTF, bandwidths are between 2nm~14nm). The bias current I_B was from 10.7 μA ($\sim 0.56I_{\text{sw}}$) to 17.7 μA ($\sim 0.92I_{\text{sw}}$) and wavelength λ was from 600 nm to 2000 nm with a 20-nm interval. In Fig. 3A, we used the same broadband source and filters in calibration to generate monochromatic light from visible to infrared and measured the photon count rate versus bias current with 71 sampling points. The reconstructed spectra are shown in Fig. 3B. The center frequencies agreed well with the referenced centers set by the AOTF. Broadband light sources were also measured by the single-pixel spectrometer (Fig. 3C). Figure 3D shows the reconstructed spectrum of the direct output from the broadband supercontinuum source (YSL SC-PRO-M) after a long-pass filter of a 650 nm cutoff wavelength. Some fine peaks within the spectrum were not resolved well, which is due to the limited bandwidth of the filter that gave uncertainty in calibrating Φ_{brd} .

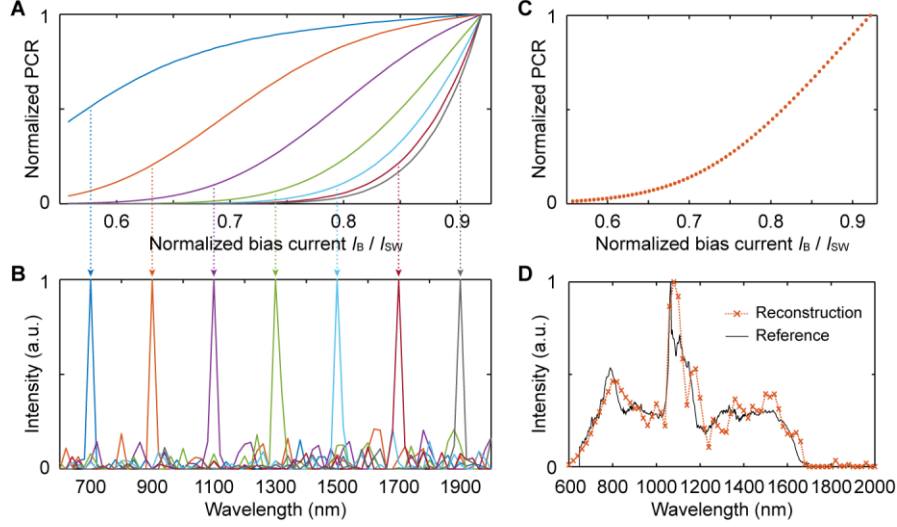


Fig. 3. Spectra reconstruction in a wide spectral range. (A) Measured PCRs for a series of monochromatic light from 700 nm to 1900 nm. (B) Reconstructed spectra (marked as the same color shown in (A)). (C) Measured PCR curves for the output from a supercontinuum source through a 650 nm long-pass filter. (D) The reconstructed spectrum from the PCR in (C). The reference spectral measured by a commercial spectrometer is shown as the black curve.

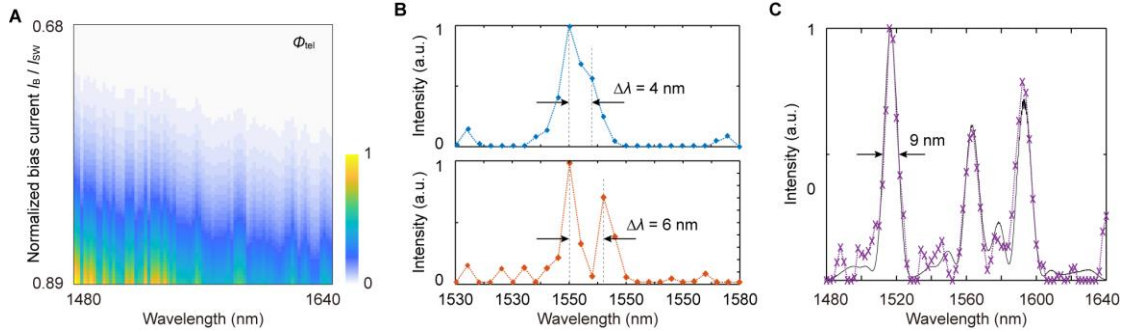


Fig. 4. Sparse spectra reconstruction in telecom band. (A) A finely calibrated responsivity matrix Φ_{tel} in the telecom band. (B) Reconstructed spectra of two mixed monochromatic light separated by 4 nm and 6 nm in telecom-band. The dotted lines mark the locations of the dual incident wavelengths. (C) The reconstructed spectra of a supercontinuum source filtered after the AOTF. Reference spectra are shown as the black curves.

The spectral resolution of the single detector spectrometer was measured at the telecom band. A finer spectral responsivity matrix Φ_{tel} (Fig. 4A) was calibrated by reducing the wavelength sampling resolution to 2 nm using a tunable laser of a narrow linewidth (Santec TSL 710), which had a size of 81×81 (I_B from $0.68I_{SW}$ to $0.89I_{SW}$, λ from 1480 nm to 1640 nm). As shown in Fig. 4B, when two incident monochromatic light were separated by 6 nm in wavelength, the spectrum reconstruction can still be done and spectral peaks were resolved. The ultimate resolution that this single-photon detector could achieve would depend on the calibration precision, measurement accuracy, and robustness of the reconstruction algorithm. Under the condition of our experiment setup, we defined

the spectral resolution of the spectrometer with the calibration matrix Φ_{tel} at telecom band was around 6 nm. We also measured the sparse spectra of the broadband light source filtered after the AOTF. Peaks centered at 1517 nm, 1563 nm, and 1593 nm with an FWHM of 9 nm were well resolved. As shown in Fig. 4C, the reconstructed spectrum is in good agreement with the reference spectrum measured by a conventional spectrometer.

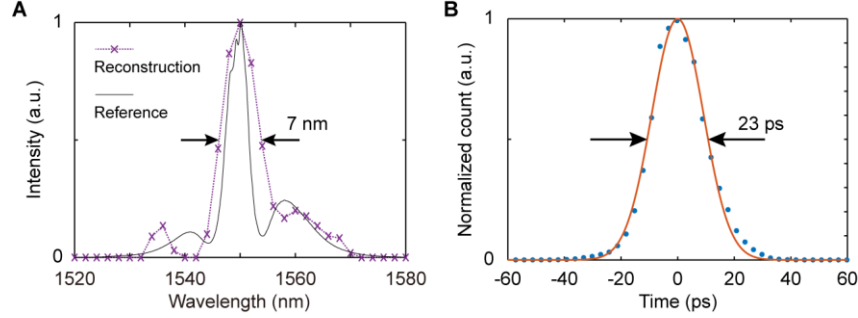


Fig. 5. Simultaneous spectral and temporal measurements of a femtosecond laser pulse. (A) The reconstructed spectra using the proposed SPS method. (B) Normalized histogram of the delay (Δt) between the photon-arrival time and a synchronized signal time. The red line shows the Gaussian fit. The SNSPD was biased at 94% I_{sw} (18 μA).

The simplification of the spectrometer reduced to one detector enables the possibility of integrating multiple functions in one system. For example, the SPS can simultaneously measure the arrival times of incident photons, which is the fundamental information for LiDAR, fluorescence lifetime imaging, and coincidence measurement in quantum optics. We demonstrated this advantage of the SPS by characterizing the spectrum and timing jitter of a mode-lock femtosecond laser (Calmar FPL02CFFPM). As shown in Fig. 5A, the laser has a spectrum of 4 nm bandwidth defined at the full-width-at-half-magnitude (FWHM), while the SPS gives a reconstructed spectrum of 7 nm bandwidth. Meanwhile, the delay between the photon arrival time and the clock reference was measured at a fixed $I_{\text{B}} = 18 \mu\text{A}$. Fig. 5B shows the histogram of the delay distribution. The timing jitter defined as the FWHM of the histogram is 23 ps, giving the timing resolution of the SPS.

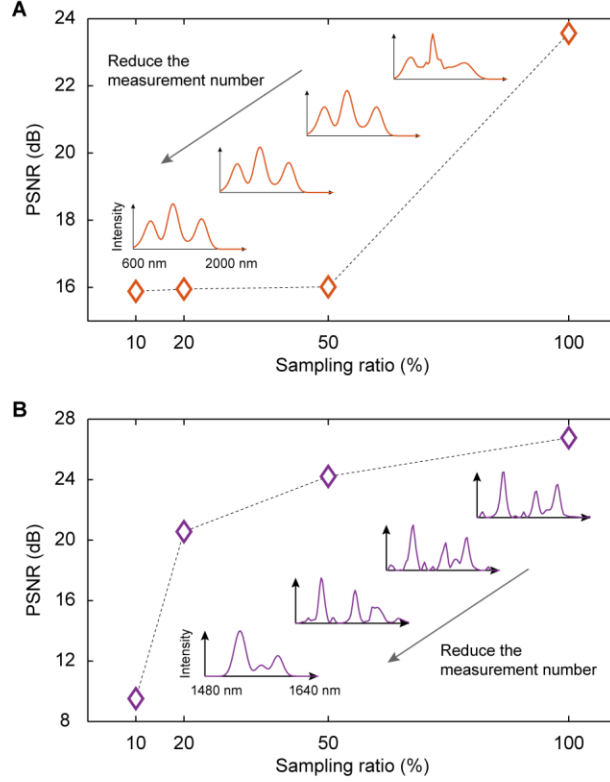


Fig. 6. Reconstruction results with different compressive ratios of sampling currents. The PSNR between reconstructed spectra and referenced spectra in the wavelength from 600 nm to 2000 nm (A) and in telecom band (B). The insert figures are the reconstruction results at the compressive ratio of 10%, 20%, 50%, 100% using the CSR algorithm.

Discussion

The single-pixel spectrometer was able to reproduce most major spectral features and differed from the reference spectral only on subtle features, which are due to measurement noise and the finite size of Φ_{brd} and Φ_{tel} . SNSPD is a photon-counting detector. Its output pulses are well above the readout noise of electronics. In our experiments, we adjusted the counting time to reach a total photon count of over 10^6 for each bias current on average. The primary measurement error was the photon shot noise from the photon counting statistic, which gives a relative counting error of less than 10^{-3} . Improving the resolution and spectrum range can be achieved by applying a finer calibration with a tunable monochromatic light of narrower linewidth. The sampling number of bias currents can be increased by programming the source supply, benefitting from the in-situ modulation ability of the detector. However, the minimum increment should be above the current noise and make the corresponding photon count curves to be distinguished under the photon counting noise.

In the single-pixel spectrometer, there is a tradeoff between the acquisition time and the spectral reconstruction accuracy, which both depend on the sampling number of bias currents and photon counting time at each bias current. Several routes exist to overcome such constraint, through either using a high-speed detector or adopt a compressive sensing algorithm. If the detector was optimized at a higher count rate, i.e. 100 MHz based on the

reported maximum count rate of an SNSPD, the acquisition time could be estimated to speed up to several seconds for having the same spectrum reconstruction quality.

Inspired by the compressive sensing method, we developed a compressive spectral reconstruction algorithm by exploiting sparse representation based on various Gaussian basis(16, 17) and the smoothing feature of natural signals (supplementary ST3). With this algorithm, we can use fewer sampling currents to reconstruct the incident spectrum with slightly reduced accuracy. For the data shown in Fig. 3D, when the sampling rate decreased to 50%, the reconstructed spectrum retained the main features as shown in Fig.6A. Compared to the result shown in Fig. 4C, when the increment of the bias current was 5 times larger, namely reducing the number of swept currents by 80%, the target spectrum can still be well recognized as shown in Fig.6B. The peak signal-to-noise ratio (PSNR) of the reconstructed spectrum was reduced from 26.78 dB to 20.57 dB. If the spectra were sparsely represented in a more sophisticated dictionary, an optimized reconstruction of an even higher-compression ratio can be expected.

In summary, we have demonstrated a single-pixel spectrometer that using only one photodetector in the absence of any wavelength multiplexing optics. Due to the avoidance of optics and detector arrays, the single-pixel spectrometer can reduce the complexity of configuration to the minimum while a sub-10 nm resolution that is comparable to other computational spectrometers has been achieved (supplementary Table S2). The performance of the spectrum measurement inherited broadband spectrum response, ultra-high sensitivity (\sim pW incident power), and 23 ps timing jitter (at 1550 nm) from an SNSPD. Our results indicate that although a single-photon detector, such as an SNSPD, has no energy resolving capacity from a single-shot measurement, with programming the measurements and combining a computational algorithm, the spectrum of the incident light can be revealed computationally. This is extremely important to detectors of broadband response at infrared, millimeter wave, terahertz, et. al., which have already been used widely in astronomical observation, biological analysis, and remote sensing. By adding parametric sweeping measurements and post signal processing, the existing hardware can gain additional spectrum information, enabling a multifunctional system. By integrating the single-pixel spectrometers and readout circuits into an array, a hyperspectral camera can be build without multiplexing optics as well.

Materials and Methods

Device fabrication

6.6-nm-thick NbN film was deposited on a 4-inch silicon wafer with a 227-nm-thick thermal oxide layer using reactive sputtering. The NbN film had a critical temperature $T_c = 7.6$ K. We spun a 76-nm-thick positive-tone resist (950PMMA A2) and then baked it at 180 °C on a hot plate for 3 min. The device structure was patterned using 100 kV electron-beam lithography. The pattern was transferred into the NbN layer using CF_4/Ar reactive-ion etching at 50 W for 70 s. The fabricated device is shown in Fig. 2A. Finally, we spun a new layer of PMMA as a protective coating.

Experimental setup

All measurements were carried out in a pulse-tube cryocooler at a temperature of 1.645 K (Fig. S1). Output pulses of the SNSPD were amplified by a cryogenic amplifier (Cosmic Microwave, CITLF3) with an integrated Bias-T. The amplifier was mounted on the 1.6 K

stage of the cryocooler and biased with a supply voltage of 1.6 V for low dissipative power (about 5.6 mW). The cryogenic amplifier provided a high signal-to-noise ratio (SNR) of electrical pulses (Fig. S2), which generated a valid registration of each output pulse by a universal counter even when the SNSPD was biased at a relatively low current.

The output light from the tunable laser was partially polarized, which affected the measurement stability of the photon count rate. To reduce the influence of polarization, on one hand, we designed a polarization-insensitive SNSPD with an orthogonal structure (Fig. 2A). On the other hand, a 4-m-long silica multimode fiber (MF) was exploited to couple the incident light to the detector, which randomizes the polarization of light (a previous work demonstrated that the ellipticity of light decreased by 70 times with a 4-m-long silica multimode fiber⁽²¹⁾). Between the detector and fiber port, a diffuser is placed to eliminate the random speckle of multimode fibers.

References and Notes

1. J. J. Dalcanton, 18 years of science with the Hubble Space Telescope. *Nature* **457**, 41-50 (2009).
2. J. Zhou, A. I. Chizhik, S. Chu, D. Jin, Single-particle spectroscopy for functional nanomaterials. *Nature* **579**, 41-50 (2020).
3. Q. Pian, R. Yao, N. Sinsuebphon, X. Intes, Compressive hyperspectral time-resolved wide-field fluorescence lifetime imaging. *Nature Photonics* **11**, 411-414 (2017).
4. D. Bannon, Cubes and slices. *Nature Photonics* **3**, 627-629 (2009).
5. N. Savage, Spectrometers. *Nature Photonics* **3**, 601-602 (2009).
6. K. D. Irwin, G. C. Hilton, D. A. Wollman, J. M. Martinis, X-ray detection using a superconducting transition-edge sensor microcalorimeter with electrothermal feedback. *Applied Physics Letters* **69**, 1945-1947 (1996).
7. J. N. Ullom, D. A. Bennett, Review of superconducting transition-edge sensors for x-ray and gamma-ray spectroscopy. *Superconductor Science and Technology* **28**, 084003 (2015).
8. B. Cabrera *et al.*, Detection of single infrared, optical, and ultraviolet photons using superconducting transition edge sensors. *Applied Physics Letters* **73**, 735-737 (1998).
9. J. Bao, M. G. Bawendi, A colloidal quantum dot spectrometer. *Nature* **523**, 67-70 (2015).
10. B. Redding, S. F. Liew, R. Sarma, H. Cao, Compact spectrometer based on a disordered photonic chip. *Nature Photonics* **7**, 746-751 (2013).
11. Z. Wang *et al.*, Single-shot on-chip spectral sensors based on photonic crystal slabs. *Nature Communications* **10**, 1020 (2019).
12. X. Zhu *et al.*, Broadband perovskite quantum dot spectrometer beyond human visual resolution. *Light: Science & Applications* **9**, 73 (2020).
13. D. M. Kita *et al.*, High-performance and scalable on-chip digital Fourier transform spectroscopy. *Nature Communications* **9**, 4405 (2018).
14. Y. August, A. Stern, Compressive sensing spectrometry based on liquid crystal devices. *Optics Letters* **38**, 4996-4999 (2013).
15. D. Pohl *et al.*, An integrated broadband spectrometer on thin-film lithium niobate. *Nature Photonics* **14**, 24-29 (2020).
16. Z. Yang *et al.*, Single-nanowire spectrometers. *Science* **365**, 1017-1020 (2019).
17. B. Cerjan, N. J. Halas, Toward a Nanophotonic Nose: A Compressive Sensing-Enhanced, Optoelectronic Mid-Infrared Spectrometer. *ACS Photonics* **6**, 79-86 (2019).
18. J. Meng, J. J. Cadusch, K. B. Crozier, Detector-Only Spectrometer Based on Structurally Colored Silicon Nanowires and a Reconstruction Algorithm. *Nano Letters* **20**, 320-328 (2020).
19. Y. Xu, Q. Lin, Photodetectors based on solution-processable semiconductors: Recent advances and perspectives. *Applied Physics Reviews* **7**, 011315 (2020).

20. B. N. Pal *et al.*, High-Sensitivity p–n Junction Photodiodes Based on PbS Nanocrystal Quantum Dots. *Advanced Functional Materials* **22**, 1741-1748 (2012).
21. F. Marsili *et al.*, Efficient Single Photon Detection from 500 nm to 5 μ m Wavelength. *Nano Letters* **12**, 4799-4804 (2012).
22. L. Chen *et al.*, Ultra-sensitive mid-infrared emission spectrometer with sub-ns temporal resolution. *Opt. Express* **26**, 14859-14868 (2018).
23. L. Ye *et al.*, Highly polarization sensitive infrared photodetector based on black phosphorus-on-WSe₂ photogate vertical heterostructure. *Nano Energy* **37**, 53-60 (2017).
24. K. Inderbitzin, A. Engel, A. Schilling, Soft X-Ray Single-Photon Detection With Superconducting Tantalum Nitride and Niobium Nanowires. *IEEE Transactions on Applied Superconductivity* **23**, 2200505-2200505 (2013).
25. E. E. Wollman *et al.*, UV superconducting nanowire single-photon detectors with high efficiency, low noise, and 4 K operating temperature. *Opt. Express* **25**, 26792-26801 (2017).
26. F. Najafi *et al.*, On-chip detection of non-classical light by scalable integration of single-photon detectors. *Nature Communications* **6**, 5873 (2015).
27. E. Reiger *et al.*, Spectroscopy With Nanostructured Superconducting Single Photon Detectors. *IEEE Journal of Selected Topics in Quantum Electronics* **13**, 934-943 (2007).
28. P. C. Hansen, REGULARIZATION TOOLS: A Matlab package for analysis and solution of discrete ill-posed problems. *Numerical Algorithms* **6**, 1-35 (1994).

Acknowledgments

We thank the other members of RISE for assistance in nanofabrication, measurements, and providing instruments. **Funding:** This work was supported by the National Key R&D Program of China Grant (2017YFA0304002), the National Natural Science Foundation (Nos. 61521001, 61801206, 61571217, 61801209 and 11227904), the Recruitment Program for Young Professionals, the Fundamental Research Funds for the Central Universities, the Priority Academic Program Development of Jiangsu Higher Education Institutions (PAPD), the Qing Lan Project and the Jiangsu Provincial Key Laboratory of Advanced Manipulating Technique of Electromagnetic Waves. **Author contributions:** L.-D.K. and Q.-Y.Z. conceived the initial idea. L.-D.K. fabricated the device, performed the experiments, analyzed data, and developed the reconstruction program. H.W., H.L., H.H., and J.C. helped with cryogenic set-up. S.-Y.G, X.-C.T., L.-B.Z., X.-Q.J., and L.K. helped with device fabrication. Q.-Y.Z., C.J., and P.W. supervised the work. L.-D.K., Q.-Y.Z., C.J., and X.-L. W. discussed the results and wrote the manuscript. **Competing interests:** The authors declare no competing financial interests. **Data and materials availability:** All data needed to evaluate the conclusions in the paper are present in the paper and the Supplementary Materials. Additional data are available from the corresponding author upon reasonable request.